Efficient Estimates of Surface Diffusion Parameters for Spatio-Temporal Resolved Virus Replication Dynamics

Markus M. Knodel *, Gabriel Wittum , Jürgen Vollmer

Posted Date: 5 January 2024

doi: 10.20944/preprints202401.0462.v1

Keywords: physical virology; hepatitis C virus (HCV); viral dynamics; within-host viral modelling; parameter estimation; 3D spatio-temporal resolved mathematical models; (surface) partial differential equations; realistic geometries; scaling analysis; geometry influence

Article

Efficient Estimates of Surface Diffusion Parameters for Spatio-Temporal Resolved Virus Replication Dynamics

Markus M. Knodel [1,†], Gabriel Wittum [1,2] and Jürgen Vollmer [3,†]

[1] Simulation in Technology, TechSim, Ölbronn-Dürrn, Germany
[2] MaS, CEMSE, KAUST, Thuwal, Saudi-Arabia
[3] Institue for Theoretical Physics, Universität Leipzig, Leipzig, Germany
† These authors contributed equally to this work.

Abstract: Advanced methods of treatment are needed to fight the threats of virus-transmitted deseases and pandemics. Often they are based on an improved biophysical understanding of virus replication strategies and processes in their host cells. For instance, an essential component of the replication of the Hepatitis C virus (HCV) proceeds under the influence of non-structural HCV proteins (NSPs) that are anchored to the endoplasmatic reticulum (ER), such as the NS5a protein. The diffusion of NSPs has been studied by in-vitro fluorescence recovery after photobleaching (FRAP) experiments. The diffusive evolution of the concentration field of NSPs on the ER can be described by means of surface partial differential equations (sufPDE). *Knodel et al, Viruses 2018, 10, 28* estimated the diffusion coefficient of the NS5a protein by minimizing the discrepancy of an extended set of sufPDE simulations and experimental FRAP time series data. Here, we provide a scaling analysis of the sufPDEs that describe the diffusive evolution of the concentration field of NSPs on the ER. This analysis provides an estimate of the diffusion coefficient that is based only on the ratio of the membrane surface area in the FRAP region and its contour length. The quality of this estimate is explored by comparison to numerical solutions of the sufPDE for a flat geometry and for ten different 3D embedded 2D ER grids that are derived from fluorescence z-stack data of the ER. Finally, we apply the new data analysis to the experimental FRAP time-series data analyzed in our previous paper, and we discuss the opportunities of the new approach.

Keywords: physical virology; hepatitis C virus (HCV); viral dynamics; within-host viral modelling; parameter estimation; 3D spatio-temporal resolved mathematical models; (surface) partial differential equations; realistic geometries; scaling analysis; geometry influence

1. Introduction

Research on virus infections is eminently important because virus infections form major challenges to animal and human health, and consequently impact global prosperity, economy, political and social systems [1–6]. Moreover, insights into the biological foundations of virus infections has revolutionized medical research by providing CRISPR/Cas [7,8] and facilitating genetic engineering [9–12]. For instance, this dichotomy is reflected in the cancer risk induced by persistent viruses [13–15], while insight in their strategies to avoid detection by the immune system unravels the working of the human immune system [16] and spawns novel approaches in cancer therapy [17–19]. In addition to concealed long-time action, viruses also trigger epidemics and pandemics [20–23] such as the recent COVID19 pandemics [24].

The present study addresses intracellular virus replication dynamics. Spatial dependence is a crucial factor in this process [24–42]. A lot of viruses cause the rearrangement of cellular membranes, and/or they induce the growth of specific regions within the host cell and inside such domains. For example, the genetic information of some viruses gets replicated inside such regions in order to prevent immune system mechanisms that strive to stop virus genome replication. Here, we

Preprints (www.preprints.org) | NOT PEER-REVIEWED | Posted: 5 January 2024 doi:10.20944/preprints202401.0462.v1

build on a framework of virus replication models for the hepatitis C virus (HCV) that aims at full 3D spatio-temporal resolution on an intracellular level [43–47]. HCV belongs to the family of plus stranded RNA (ss(+)RNA) viruses [27,48] such as Dengue and Yellow fever viruses (DNFV and YFV) [27,32], and the Coronaviridiae such as SarsCov1 and SarsCov2 [24]. The aim of the project is to develop an "in silico microscope" for direct comparisons between experiment and simulation of biophysical models of intracellular virus replication. The present approach augments this approach by estimates of material parameters derived directly from the experimental data.

The nonstructural proteins (NSPs) of the HCV virus govern the replication of the HCV genome (viral RNA - vRNA) [27,49]. Directly after their cleavage from the viral polyprotein, which is translated at the ribosomes from the information stored within the vRNA attached to the ribosomes, the NSPs anchor to the ER surface [27,28,30,48,50,51]. Thus, the movement of the NSPs is restricted to the ER surface, which is a 2D curved manifold embedded in 3D. Refs. [43–47] described the evolution of the vRNA cycle by surface partial differential equations (sufPDEs). These equations were evaluated numerically on reconstructed geometry grids describing the ER and membranous web (MW) regions. They are represented as subdomains of a computational mesh that is derived from fluorescence stacks of stained cell structures. Surface diffusivity of NSPs on the ER is an important material parameter of the models that is needed to arrive at quantitative predictions of the rates of the biochemical reaction kinetics of processes located on the ER [50,52–55]. In a recent study [45] the diffusion constant of the NS5a protein (a major HCV NSP) was estimated based on 20 time series of fluorescence recovery after photobleaching (FRAP) experiments [50,52,53]. For each of these time series the diffusion coefficient was estimated by obtaining an optimal match with the numerical solutions of the sufPDE for each of 10 different ER geometries [25]. This procedure was chosen because the geometry of the ER is not recorded in FRAP experiments [50]. Finding the optimal matching by the Gauss-Newton procedure involved about 4×10^4 simulations with different sets of geometries and material parameters, and about 4 Million of core hours at the HLRS Stuttgart hazel hen supercomputer [46]. It the end, the global optimum was obtained as a Bayesian average [45].

In the present paper we provide a scaling analysis [56,57] of the solutions of the sufPDE. We explore how the recovery of bleaching is impacted by the surface geometry, and we establish how the surface diffusivity can be inferred based on a scaling plot. This approach assumes that the diffusion coefficient is the same for all experiments with the same cell type, and that the difference of the FRAP time series is exclusively due to different shapes of the ER. It suggests an algorithm to determine the surface diffusivity that relies solely on knowledge of the initial fluorescence and a length scale characterizing the geometry of the ER. These conclusion are underpinned by simulations that account for the complex geometric and topological structures of ERs. Finally, the application of the new data-analysis method is demonstrated by revisiting the FRAP time series data analyzed in [45,50].

This paper is organized as follows: In the materials and methods Sect. 2, we revisit the biological problem, the experimental measurements, and the numerical methods. Section 3 provides a scaling analysis of the model equations. In Sect. 4 we present a novel approach to determine the diffusivities of surface proteins based on FRAP data, and we compare its results to those obtained in Ref. [45]. Finally, in Sect. 5, we discuss and summarize our main results.

2. Revisiting Materials and Methods

The present paper addresses the analysis of in-vitro fluorescence recovery after photobleaching (FRAP) [52,53]. The measurements provide direct access to transport properties of fluorescently labeled substances in the cell.

2.1. FRAP Experiments

Here we consider FRAP experiments [50] where NS5A proteins are marked by fluorescent dye. The proteins reside on the ER surface in liver cells. The cell is prepared in a state where the protein is distributed (and fluoresces) homogeneously. In Fig. 1 the ER appears as a bicontinuous structure

Preprints (www.preprints.org) | NOT PEER-REVIEWED | Posted: 5 January 2024 doi:10.20944/preprints202401.0462.v1

colored in red and blue. The ER has a height of a few pore diameters and large lateral extension. The experiment starts by applying a bright laser pulse applied to a small and sharply confined spatial region. In Fig. 1 this region is colored in red. The pulse bleaches the dye and hence quenches the fluorescence in this region. In the following these regions will be denoted as the FRAP region of interest (FRAP ROI) $\mathcal{F}$. This region has the shape of a cylinder, with a height that amounts to the thickness of the ER, $H \simeq 3.5\,\mu\text{m}$, and a circular cross section of $A = \pi R^2$ with $R \simeq 3.5\,\mu\text{m}$.

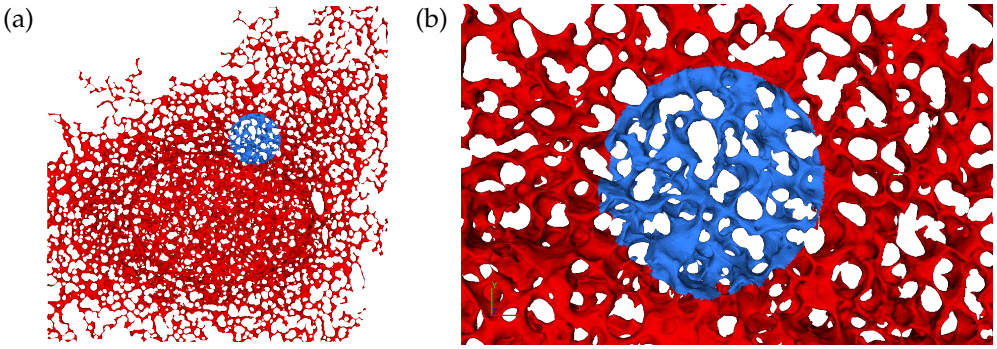

structure	location	$\lvert\mathcal{F}\rvert$ / [µm^2]	$\lvert\partial\mathcal{F}\rvert$ / [µm]	$\lvert\mathcal{U}\rvert$ / [µm^2]
M1	*a*	152.4	89.1	6335
	b	135.3	75.3	6351
M2	*a*	95.8	55.1	468
	b	115.7	59.6	448
M3	*a*	298.7	171.4	9858
	b	293.7	165.3	9863
M4	*a*	87.3	50.9	5120
	b	76.7	48.2	5130
M5	*a*	176.8	113.0	4540
	b	117.6	66.9	4599
disc		38.0	22.1	2790

Figure 1. Surface mesh of a reconstructed ER geometry. (**a**) Computational domain used for the simulations of the FRAP experiments of NS5A. The displayed ER has a maximum thickness of about 4.8 µm, which amounts to only a few pore diameters, and the present view has a lateral extension of 46 µm × 46 µm. The unbleached region $\mathcal{U}$ is displayed in dark blue, and the FRAP region $\mathcal{F}$ used for bleaching in red. (**b**) Magnification around the FRAP region $\mathcal{F}$ with an extension of 19.2 µm × 10.9 µm, and a maximum thickness of about 3.5 µm. The FRAP region $\mathcal{F}$ has a surface area of $A = 38\,\mu\text{m}^2 \simeq \pi\,(3.5\,\mu\text{m})^2$ in the 2D projection plane. The table provides the relevant properties of the reconstructed ER geometries adopted in the present study. Details on the reconstruction and representation of the surface meshes are provided in [45].

After bleaching the diffusive rearrangement of NS5A between the region and its environment is recorded by tracking the recovery of fluorescence. Fluorescence recovers due to the influx of NS5A proteins labeled with operational dye molecules from the surrounding unbleached region $\mathcal{U}$. The recovery is followed by inducing dye fluorescence by repetitive application of a second (soft) laser beam. Representative measurement signals are shown by the data points in Fig. 2. The initial recovery up to a level of 0.35 proceeds within a few seconds. Subsequently, the experimental signal keeps rising slowly. However, even the soft laser beam causes photobleaching, and this photobleaching is slowly extinguishing the fluorescence signal. Full details are provided in Ref. [45].

Preprints (www.preprints.org) | NOT PEER-REVIEWED | Posted: 5 January 2024 doi:10.20944/preprints202401.0462.v1

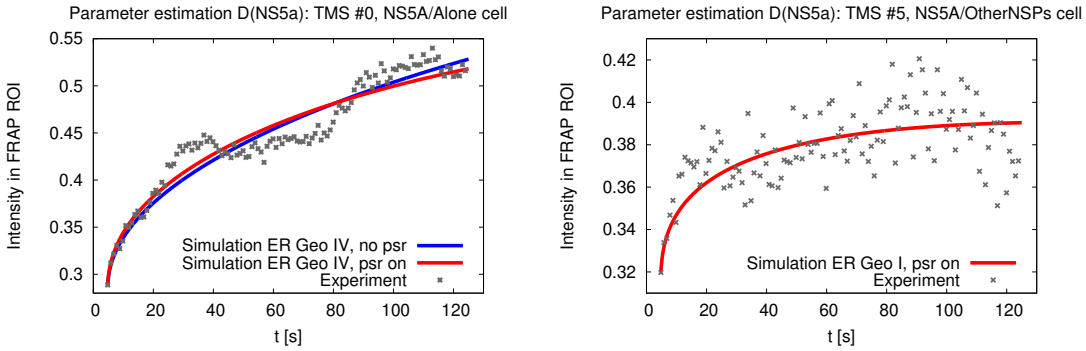

		quantity unit	$i_0^{\mathcal{F}}$	$i_0^{\mathcal{U}}$	r_p $[\mathrm{s}^{-1}]$	D $[\mu\mathrm{m}^2\,\mathrm{s}^{-1}]$	
left	M4a		0.289	0.847	0	0.268	blue
					1.1×10^{-3}	0.0346	red
right	M1a		0.319	0.932	1.56×10^{-3}	0.0107	red

Figure 2. Experiment (dots) and simulations (solid lines) of the FRAP signal for two different cell lines where one expects different surface diffusivities D. The blue and red lines show simulation results where photobleaching is neglected and for a finite quench rate, respectively. The geometry of the ER of the cells used in the experiments is not known. The simulations were performed for the geometry M4a (left) and M1a (right), respectively. The initial conditions and parameters adopted in the simulations are provided in the table below the plots. [The Figure was initially published as Fig. 5 and Fig. 6 in Ref. [45]].

Numerical tests of our theoretical considerations will be compared to simulations performed for diffusion on reconstructions of the ER geometry. An example is provided in Fig. 1. The ER geometries will be denoted as M1 to M5. For each of them we consider 2 distinct locations of the FRAP region of interest. This distinction will be marked by *a* and *b*, respectively. Hence, for the simulations we consider 10 ER structures in total. Moreover, in order to explore the impact of the bicontinuous structure of the ER, we also perform simulations on a flat disk. This structures will be denoted as disk. The relevant material parameters of the structures are provided in the table in Fig. 1. A detailed description of the structures and the numerical method has been provided in Ref. [45].

2.2. Mathematical Model of NS5A Diffusion

We express the dynamics of NS5A fluorescence in terms of the intensity density

$$i_{\mathrm{ns5a}}(t,\mathbf{x}) \propto c_{\mathrm{ns5a}}(t,\mathbf{x})$$

that is proportional to the concentration $c_{\mathrm{ns5a}}(t,\mathbf{x})$ anchored in the ER. We consider 5 ER geometries that are reconstructed based on experimental data. The surfaces are represented as triangulated manifolds with a resolution of about 10^6 nodes [45]. Figure 1 shows an example of such a geometric setup. The ER [25,58,59] comprises a bicontinuous structure with a characteristic pore diameter of 1 µm. It has a thickness of a few pore diameters, and a lateral extension of about 50 pore diameters in the other two directions. The overall surface area of the membrane comprising the ER is of the order of $|\mathcal{U}| \simeq 5000\,\mu\mathrm{m}^2$. The specific values for the structures considered in the present study are provided in the table in Fig. 1. Full details concerning the investigated structures are provided in [43,45,46].

The evolution of the protein on the ER surface domain is described by a surface PDE (sufPDE)

$$\frac{\mathrm{d}}{\mathrm{d}t} i_{\mathrm{ns5a}}(t,\mathbf{x}) - D\Delta_{(\mathrm{T})} i_{\mathrm{ns5a}}(t,\mathbf{x}) = -\, r_p\, i_{\mathrm{ns5a}}\big|_{\mathcal{F}} \quad , \qquad \forall \mathbf{x} \in \mathcal{F} \cup \mathcal{U}. \tag{1}$$

Preprints (www.preprints.org) | NOT PEER-REVIEWED | Posted: 5 January 2024 doi:10.20944/preprints202401.0462.v1

where the Laplace-Beltrami operator $\Delta_{(\mathrm{T})}$ is the projection of the Laplace operator to the tangential space of the two dimensional ER-hypersurface $\mathcal{F} \cup \mathcal{U}$. It models diffusion, analogously to a Laplace operator for diffusion in Euclidean space. The right-hand side of the equation accounts for the intensity reduction due to quenching of the dye in the course of the the intensity measurement with the soft laser.

The present analysis is adopting simulations without quenching $r_p = 0\,\mathrm{s}^{-1}$, and with a quench rate $r_p \simeq 0.0020\,\mathrm{s}^{-1}$ that is slightly larger than the values $0.0011\,\mathrm{s}^{-1}$ and $0.0016\,\mathrm{s}^{-1}$ reported for NS5A/Alone and NS5A/OtherNSPs cells, respectively [45].

The surface diffusion coefficient D is varied in the range of $5 \times 10^{-4} \ldots 1 \times 10^{-1}\,\mu\mathrm{m}^2/\mathrm{s}$. In order to match the experimental setup, initial conditions for Eq. (1) are provided independently for the bleached ($\mathcal{F}$) and unbleached ($\mathcal{U}$) regions

$$i_{\mathrm{ns5a}}(t_0, \mathbf{x}) = \begin{cases} i_0^{\mathcal{F}}\,, & \forall \mathbf{x} \in \mathcal{F}\,, \\ i_0^{\mathcal{U}}\,, & \forall \mathbf{x} \in \mathcal{U}\,. \end{cases} \tag{2}$$

For the comparison with the experimental intensity in $\mathcal{F}$, we define the integrated normalized luminosity

$$I(t) = \langle i_{\mathrm{ns5a}}(t, \mathbf{x}) \rangle_{\mathcal{F}} = \frac{\iint_{\mathcal{F}} \mathrm{d}S\, i_{\mathrm{ns5a}}(t, \mathbf{x})}{\iint_{\mathcal{F}} \mathrm{d}S} \tag{3}$$

where $\mathrm{d}S$ denotes surface area elements on the ER.

Figure 3 displays a screenshot of a simulation movie for the NS5A dynamics on the ER surface mimicking a FRAP experiment. The simulation movie itself is attached as supplemental movie to this study.

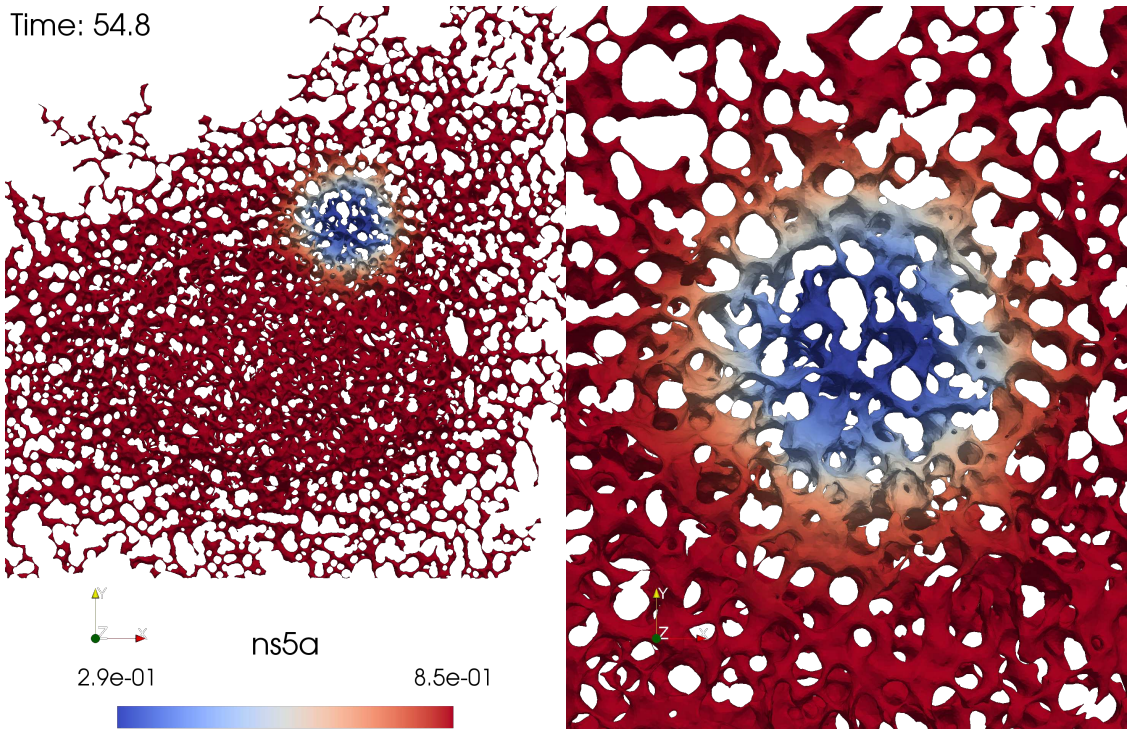

Figure 3. Screenshot of the evaluation of NS5A FRAP experiment simulation based on sufPDE description, Eq. (1), on an ER surface: (left) total view, (right) zoom into FRAP ROI event. The complete movie is attached as supplemental material to this study.

Preprints (www.preprints.org) | NOT PEER-REVIEWED | Posted: 5 January 2024 doi:10.20944/preprints202401.0462.v1

2.3. Parameter Estimation Technique Employed in Ref. [45]

The authors of Ref. [45] adopted a Gauss-Newton recursion scheme to determine the value of the diffusion constant D that provided the best match of the the numerically computed intensity and a FRAP scan covering 125 seconds of experimental data. Typically, around 50 simulation runs were required to reach convergence. Each of these has a resolution of about 1 Million degrees of freedom [46] at base level. The value of the surface diffusion coefficient was estimated from this data by minimizing the mismatch over all combinations of experimental data and numerical time series [45]. All in all, this took about 4 Million of core hours on the supercomputer hazel hen at the HLRS Stuttgart [46].

3. Scaling Analysis

In this section we discuss the non-dimensionalization of the sufPDE (1), and the scaling properties of its solutions. As a first step we establish the equations describing the intensity in $\mathcal{F}$.

3.1. Scaling Analysis of the FRAP ROI Intensity

In order to discuss the solutions of Eq. (1) we introduce the surface area in the hole,

$$|\mathcal{F}| = \iint_{\mathcal{F}} \mathrm{d}S\,.$$

and the space-dependent absorption rate

$$\gamma(\mathbf{x}) = r_p\,\chi(\ell(\mathbf{x}))$$

where $\ell(\mathbf{x})$ is the signed distance of $\mathbf{x}$ to the boundary $\partial\mathcal{F}$ of $\mathcal{F}$ (with negative values denoting positions inside $\mathcal{F}$), and

$$\chi(\ell) = \begin{cases} 1 & \text{for} \quad \ell \le 0 \\ 0 & \text{for} \quad \ell > 0 \end{cases}$$

With these we write Eq. (1) as

$$\mathrm{e}^{-\gamma(\mathbf{x})\,t}\,\frac{\mathrm{d}}{\mathrm{d}t}\left(\mathrm{e}^{\gamma(\mathbf{x})\,t}\;i_{\mathrm{ns5a}}(t,\mathbf{x})\right) = D\,\Delta_{(\mathrm{T})} i_{\mathrm{ns5a}}(t,\mathbf{x}) \tag{4}$$

Multiplying by $\exp\big(\gamma(\mathbf{x})\,t\big)$, dividing by $\mathcal{A} = |\mathcal{F}|$, and integrating both parts over $\mathcal{F}$ provides

$$\begin{aligned}
\frac{\mathrm{d}}{\mathrm{d}t}\left(\mathrm{e}^{r_p\,t}\;I(t)\right) &= \frac{D}{|\mathcal{F}|}\iint_{\mathcal{F}} \mathrm{d}S\,\mathrm{e}^{\gamma(\mathbf{x})\,t}\,\Delta_{(\mathrm{T})} i_{\mathrm{ns5a}}(t,\mathbf{x}) \\
&= \frac{D}{|\mathcal{F}|}\;\mathrm{e}^{r_p t}\;\iint_{\mathcal{F}} \mathrm{d}S\,\nabla_{(\mathrm{T})}\,\nabla_{(\mathrm{T})} i_{\mathrm{ns5a}}(t,\mathbf{x}) \\
&= \frac{D}{|\mathcal{F}|}\;\mathrm{e}^{r_p t}\;\oint_{\partial\mathcal{F}} \mathrm{d}\hat{\mathbf{n}}\cdot\nabla_{(\mathrm{T})} i_{\mathrm{ns5a}}(t,\mathbf{x})
\end{aligned} \tag{5}$$

Here we first used that $\gamma(\mathbf{x}) = r_p$ takes a constant value on $\mathcal{F}$, and then we adopted Gauss's theorem to express the integral over $\mathcal{F}$ as an integral over its surface $\partial\mathcal{F}$.

Equation (5) must be solved for the initial condition

$$I(0) = \langle i_{\mathrm{ns5a}}(t_0,\mathbf{x})\rangle_{\mathcal{F}} = i_0^{\mathcal{F}}\,.$$

Preprints (www.preprints.org) | NOT PEER-REVIEWED | Posted: 5 January 2024 doi:10.20944/preprints202401.0462.v1

3.2. Scaling for Negligible Photobleaching

In the absence of photobleaching, $r_p \simeq 0$, Equation (5) reduces to

$$\frac{R^2}{D}\frac{\mathrm{d}}{\mathrm{d}t}I(t) = \frac{R^2}{|\mathcal{F}|}\oint_{\partial\mathcal{F}} \mathrm{d}\hat{\mathbf{n}}\cdot\hat{\nabla}_{(\mathrm{T})} i_{\mathrm{ns5a}}(t,\mathbf{x})\,, \tag{6a}$$

$$\text{with}\quad \frac{R^2}{D}\frac{\mathrm{d}}{\mathrm{d}t} i_{\mathrm{ns5a}}(t,\mathbf{x}) = R^2\,\Delta_{(\mathrm{T})} i_{\mathrm{ns5a}}(t,\mathbf{x})\,. \tag{6b}$$

We non-dimensionalize the equations by adopting the radius R of the FRAP region as length scale and the dimensionless time $\tau = D(t-t_0)/R^2$. Moreover, we note that the equations (6) are liner. As a consequence, there is a superposition principle and one can account for the different values of $i_0^{\mathcal{U}}$ and $i_0^{\mathcal{F}}$ in the initial condition by considering the normalized intensity $\tilde{I}(\tau) = (I(t)-I_0)/(|i_0^{\mathcal{U}} - i_0^{\mathcal{F}}|)$ (see the chapter on Greens functions in Ref. [60]).[1] As a consequence, the reduced intensity takes same evolution for every geometry of the ER, irrespective of the value of the diffusion coefficient and the initial condition.

This prediction is tested in Fig. 4 where we plot data for the different geometries of the ER and for the 2D planar geometry. For each geometry the data for different diffusion coefficients collapse on a master curve. However, data for different geometries lie on distinctly different curves. The values of data for different ER geometries vary by about 20%, and those for the disk geometry (uppermost curve in the plot) take noticeably higher values. This highlights the importance of the ER geometry for the FRAP relaxation.

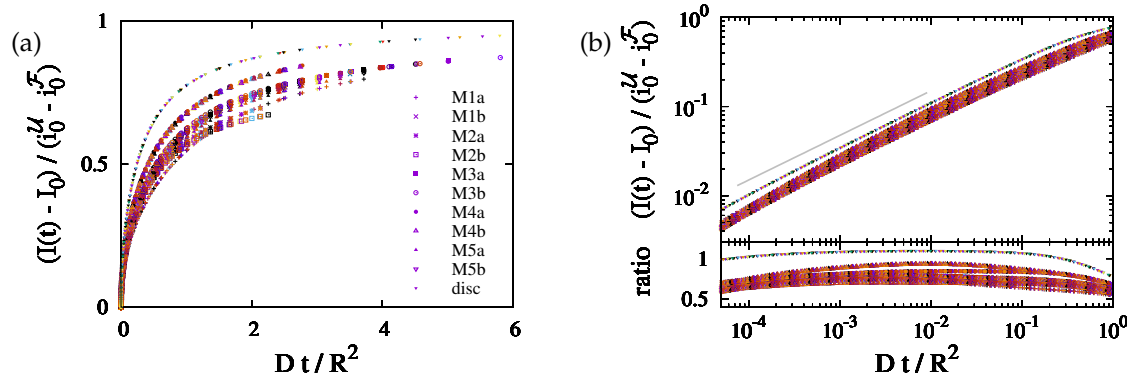

Figure 4. Data collapse for the reduced density $(I(t) - I(0))/(|i_0^{\mathcal{U}} - i_0^{\mathcal{F}}|)$ as function of the dimensionless time $D\,t/R^2$. Different colors refer to different values of D, that take values in $D \in \{5\times10^{-4}\,\mu\mathrm{m}^2/\mathrm{s}\,,\ 1.5\times10^{-3}\,\mu\mathrm{m}^2/\mathrm{s}\,,\ \cdots\,,\ 0.1\,\mu\mathrm{m}^2/\mathrm{s}\}$. The symbols refer to different geometries, as specified in the legend. (a) Simulation data with a linear scale. There are different curves for each geometry, but for any given geometry the data with different D collapse on a single line. (b) The upper panel provides a double-logarithmic plot of the data shown in (a). The lower panel shows the ratio of the data and $\sqrt{D\,t/R^2}$. To a good approximation it is a horizontal line. Hence, the data lie on a power law with exponent 1/2, where the ratio provides the prefactor of the power law. For the planar geometry the prefactor takes a value slightly larger than one. For the bicontinuous structures it differs for each geometry, with values in the rage between 0.5 and 0.8.

[1] Note that initially the density $i_0^{\mathcal{F}}$ in $\mathcal{F}$ is uniform such that it agrees with its average value I_0.

Preprints (www.preprints.org) | NOT PEER-REVIEWED | Posted: 5 January 2024 doi:10.20944/preprints202401.0462.v1

Figure 4 suggests that the relaxation of the reduced density has a time dependence proportional to the square root of the dimensionless time. We will show now that this is an immediate consequence of the form of the initial condition.

For the initial condition, Eq. (2), the intensity $i_{\mathrm{ns5a}}(t, \mathbf{x})$ takes the form of the step function,

$$i_{\mathrm{ns5a}}(t_0, \mathbf{x}) = \frac{i_0^{\mathcal{U}} + i_0^{\mathcal{F}}}{2} - \chi\big(\ell(\mathbf{x})\big)\, \frac{i_0^{\mathcal{U}} - i_0^{\mathcal{F}}}{2}\,.$$

For early times the flow is orthogonal to the surface, i.e., curvature and topology of the surface may still be neglected. The gradient of the density therefore follows the evolution of diffusive decay of a step function in one dimension[2]

$$\nabla_{(\mathrm{T})} i_{\mathrm{ns5a}}(t_0, \mathbf{x}) = \frac{i_0^{\mathcal{U}} - i_0^{\mathcal{F}}}{2\sqrt{4\pi\, D\, t}}\, \exp\left(-\frac{\ell^2}{4D\, t}\right) \tag{7}$$

Right on the interface, we have $\ell = 0$, and the exponential function takes the value of one. Hence, Eq. (6a) reduces to

$$\frac{\Lambda^2}{D}\frac{\mathrm{d}}{\mathrm{d}t} I(t) = \frac{i_0^{\mathcal{U}} - i_0^{\mathcal{F}}}{2}\sqrt{\frac{\Lambda^2}{D\, t}} \qquad \text{with} \qquad \Lambda = \sqrt{4\pi}\, \frac{|\mathcal{F}|}{|\partial\mathcal{F}|} \tag{8}$$

Integrating time from $t_0 = 0$ till t provides

$$\frac{I(t) - I_0}{i_0^{\mathcal{U}} - i_0^{\mathcal{F}}} = \sqrt{\frac{D\, t}{\Lambda^2}} \tag{9}$$

This result explains the square root dependence of the intensity observed in Fig. 4, and it provides the leading order dependence of the dependence on the surface geometry via the characteristic length scale $\Lambda = \sqrt{4\pi}\, |\mathcal{F}|/|\partial\mathcal{F}|$.

The prediction is tested in Fig. 5(a). At late time the recovery is still considerably impacted by the ER geometry. The curves for different geometries differ by up to 25%. However, at early time the transformation from a time scale Dt/R^2 to Dt/Λ^2 provides a very nice data collapse for the ER geometries. For a perfect fit the ratio of the data and $\sqrt{D\, t/\Lambda^2}$ must be one. For our simulations it takes a value close to $\phi_- = 1.25$. We attribute this difference to the impact of the nontrivial curvature of the border of $\mathcal{F}$.[3]

---

[2] The solution is obtained as follows: The step function is the derivative of a delta function. Consequently, its time evolution amounts to the derivative of the Greens function of diffusion, which is a Gaussian function [60].

[3] The solution Eq. (7) applies when the normal direction $\hat{n}$ at the interface of $\mathcal{F}$ does not change when moving along the interface. This holds for a straight line in a plane, and for a section vertically through a cylinder. For the surface of the disks this condition is always violated, such that the prefactor takes a values substantially larger than one. For the surface of $\mathcal{F}$ it applies to a good approximation at *some* place. Hence, the prefactor takes a values closer to one than for a disk.

Preprints (www.preprints.org) | NOT PEER-REVIEWED | Posted: 5 January 2024 doi:10.20944/preprints202401.0462.v1

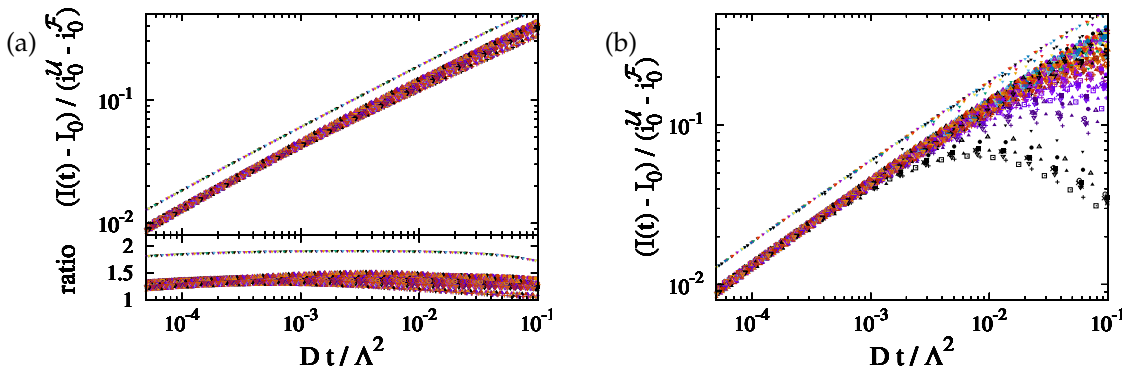

Figure 5. (a) Master plot, Eq. (9), for the data shown in Fig. 4(b). The values of Λ depend on the geometry. This reduces the variance of the prefactors by roughly a factor of two. For the ER geometries they take values of about $\phi_- = 1.25(7)$. For a 2D disk it is close to 1.8. (b) The same master plot for data with non-vanishing photobleaching, r_p. At early times the data still follow the prediction, but now there is a cross-over to a regime where photobleaching has a severe impact.

3.3. Accounting for Photobleaching

The data collapse at early times also holds for systems with bleaching (Fig. 5(b)). However, at late times these systems cross over to a decay of the intensity that is caused by bleaching. In order to gain insight into this behavior we insert Eq. (7) into Eq. (5),

$$\frac{1}{r_p}\frac{\mathrm{d}}{\mathrm{d}t}\left(\mathrm{e}^{r_p t}\, I(t)\right) = \frac{K}{\sqrt{r_p t}}\,\mathrm{e}^{r_p t} \qquad \text{with} \qquad K = \sqrt{\frac{D}{\Lambda^2 r_p}}\,\frac{i_0^{\mathcal{U}} - i_0^{\mathcal{F}}}{2} \tag{10}$$

where K is a dimensionless constant. This equation can be integrated

$$\mathrm{e}^{r_p t}\, I(t) - I_0 = K\int_0^{r_p t}\mathrm{d}\tau\,\frac{\mathrm{e}^{\tau}}{\sqrt{\tau}} = K\int_0^{\mathrm{i}\sqrt{r_p t}}\mathrm{d}\theta\,(-2\mathrm{i})\,\mathrm{e}^{-\theta^2} = -K\,\mathrm{i}\sqrt{\pi}\,\operatorname{erf}(\mathrm{i}\sqrt{r_p t})$$

where $\operatorname{erf}(x)$ is the error function. Rearranging the terms provides

$$\frac{I(t) - I_0\,\mathrm{e}^{-r_p t}}{K} = +\frac{\sqrt{\pi}}{\mathrm{i}}\,\operatorname{erf}(\mathrm{i}\sqrt{r_p t})\,\mathrm{e}^{-r_p t} \tag{11}$$

This prediction is tested in Fig. 6(a). Indeed we observe a data collapse. It features a cross over between different power laws for small and large values of $r_p t$.

For $r_p t \ll 1$ the exponential function and the error function on the right-hand side can be expanded in a power series. This entails a square-root dependence for early times,

$$\frac{I(t) - I_0\,\mathrm{e}^{-r_p t}}{K} \simeq 2\sqrt{r_p\, t}\,\left(1 - \frac{2}{3}\,r_p t + \mathcal{O}(r_p t)^2\right) \tag{12}$$

This is in line with Fig. 6(a) where the data for small $r_p t$ lie close to $2\,\phi_-\sqrt{r_p t}$ with $\phi_- = 1.25$. Here, the correction factor ϕ_- accounts for the curvature effects reported in Fig. 5(a).

To find the asymptotics for $r_p t \gg 1$ we observe that

$$\frac{I(t) - I_0\,\mathrm{e}^{-r_p t}}{K} = \int_0^{r_p t}\mathrm{d}\tau\,\frac{\mathrm{e}^{\tau - r_p t}}{\sqrt{\tau}} = \int_0^{r_p t}\mathrm{d}\tau\,\frac{\mathrm{e}^{-\tau}}{\sqrt{r_p t - \tau}} = \frac{1}{\sqrt{r_p t}}\,\left(1 + \frac{1}{2 r_p t} + \cdots\right)$$

Preprints (www.preprints.org) | NOT PEER-REVIEWED | Posted: 5 January 2024 doi:10.20944/preprints202401.0462.v1

This is in line with the data collapse in Fig. 6(a) where the data for large $r_p t$ lie close to $2\,\phi_+/\sqrt{r_p t}$ with $\phi_+ = 2$. Here, a correction term, ϕ_+, of the prefactor is expected since Eq. (7) is based on an approximation that applies only for early times.

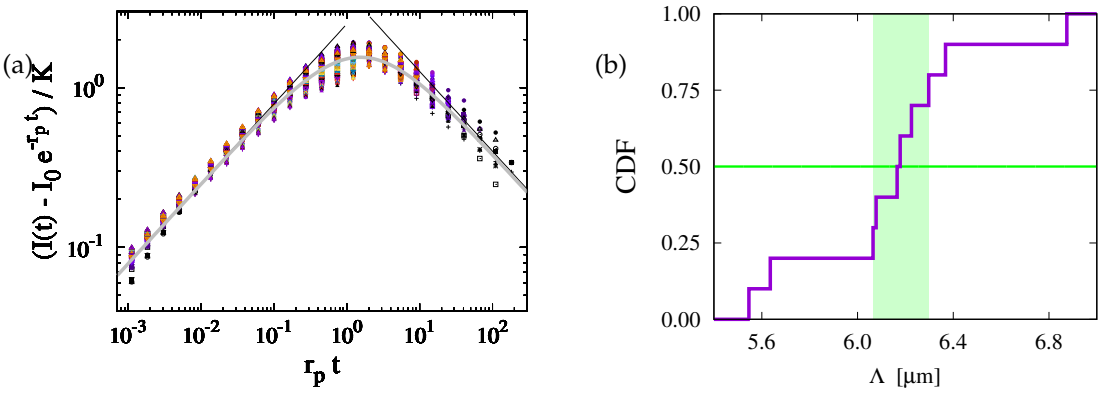

Figure 6. (a) Data collapse of all data on a master curve predicted by Eq. (11). There is a very good collapse for small times, and the cross-over due to photobleaching is also accounted for. The two straight gray lines show the function $2\,\phi_-\sqrt{r_p t}$ and $2\,\phi_+/\sqrt{r_p t}$ with $\phi_- = 1.25$ and $\phi_+ = 2$, respectively. An extrapolation that agrees very well with the observed data is provided by $2\,\phi_-\,\phi_+\sqrt{r_p t}/(\phi_+ + \phi_-\,r_p t)$ (thick solid gray line). (b) cumulative distribution of the values of $\Lambda = \sqrt{4\pi}|\mathcal{F}|/|\partial\mathcal{F}|$. For $\mathcal{F}$ with a radius of $R = 3.5\,\mu$m in the presently considered ER geometries the values of Λ are sharply centered in a narrow interval with a width of 0.3 µm (shaded region) around a median of $\bar{\Lambda} \simeq 6.17\,\mu$m.

4. Novel Approaches to analyze FRAP Data

The analysis of Sect. 3 suggest two approaches for a data analysis of FRAP data. We explore the chances and challenges provided by the insights of Sect. 3 by revisiting the analysis of the data introduced in Fig. 2. The best fits of the analysis of Ref. [45] and those that will be derived in the following are summarized in Tab. 1.

Table 1. Comparison of estimated quench rates and diffusion coefficients for the cell lines introduced in the left and right panel of Fig. 2. The first row shows the results of Ref. [45]. The other two rows are obtained by two different approaches for the data analysis that are discussed in Sects. 4.1 and 4.2 of the present study. Their respective results are summarized in Figs. 7 and 8.

		cell line 1		cell line 2	
	quantity	r_p	D	r_p	D
method	unit	s^{-1}	$\mu m^2/s$	s^{-1}	$\mu m^2/s$
Ref. [45]		0.0011	0.033	0.0016	0.0077
Eq. (9)		—	0.05	—	0.015
Eq. (11)		0.004(1)	0.075(15)	0.004(1)	0.034(13)

Preprints (www.preprints.org) | NOT PEER-REVIEWED | Posted: 5 January 2024 doi:10.20944/preprints202401.0462.v1

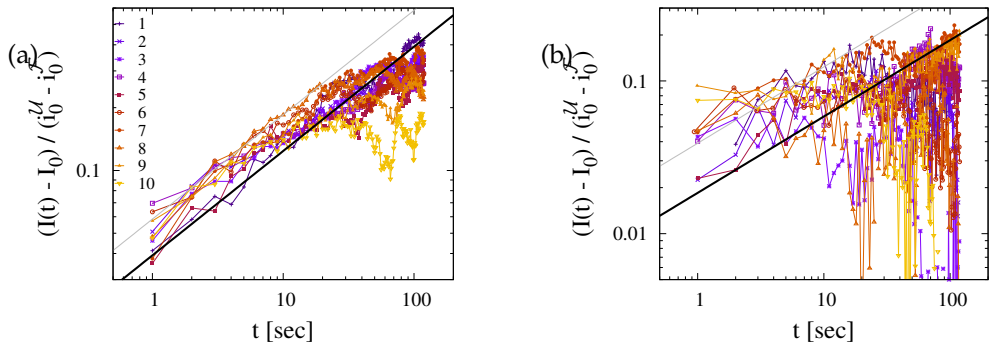

Figure 7. Fitting the diffusion constant to experimental data values. Panels (a) and (b) show data for the two cell lines introduced in Fig. 2 where the left-hand side of Eq. (13) is plotted as function of time. The solid black lines show the prediction of Eq. (9) with correction factor $\phi_- = 1.25$ when it is evaluated for the data obtained in Ref. [45]. The gray lines provide the dependences by the best fits obtained for the values of D obtained in Sect. 4.2. See Tab. 1 for a summary of these values.

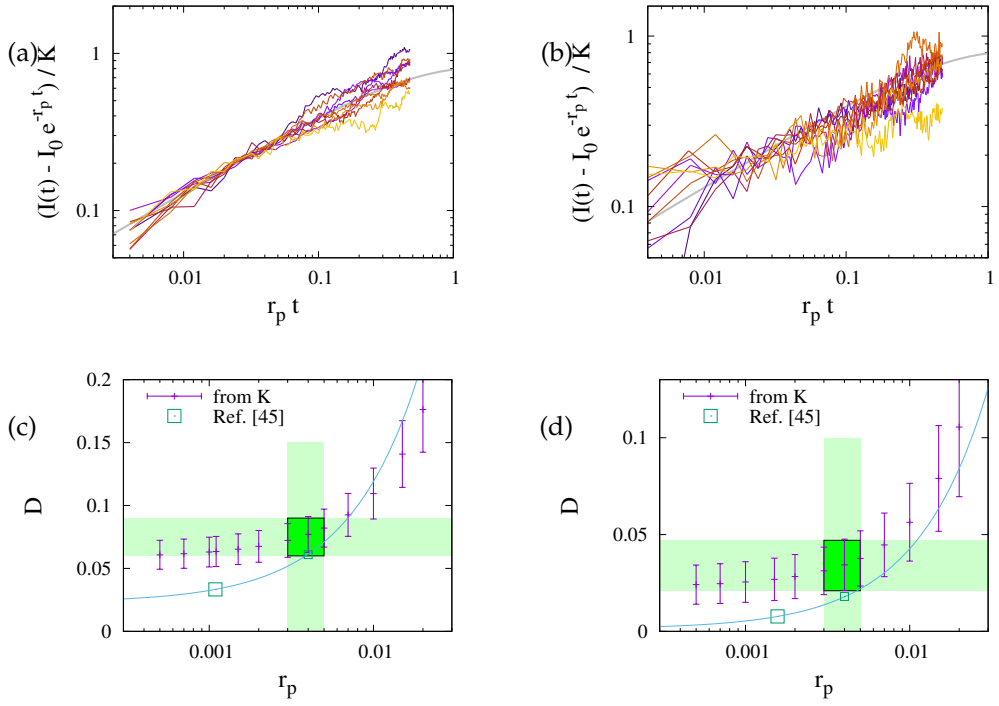

Figure 8. Analysis of the experimental data considered in Fig. 7 that is based on Eq. (14). Panels (a) and (b) show data for the two cell lines together with the best fits for $r_p = 4 \times 10^{-3}\,\mathrm{s}^{-1}$ where the fit proceeds through the expectation of the distribution of data for large values of $r_p t$. Panels (c) and (d) show the prediction of D obtained by the analysis of the factor K. The small points with error bars refer to our present data. The points indicated by large boxes provides the value suggested in Ref. [45], and the solid line shows the extrapolation to other quench rates described in the appendix of that paper. For the quench rates obtained in the present analysis the predictions agree within the error margins.

Preprints (www.preprints.org) | NOT PEER-REVIEWED | Posted: 5 January 2024 doi:10.20944/preprints202401.0462.v1

4.1. Analysis Based on Eq. (9)

The first option is to collect a vast amount of data for times where bleaching still has negligible impact. To work out this condition we expand the exponential function on the left-hand side of Eq. (12), insert the expression of K, and rearrange terms. This provides Eq. (9) and its leading order corrections

$$\begin{aligned}\frac{I(t)-I_0}{i_0^{\mathcal{U}}-i_0^{\mathcal{F}}} &\simeq \sqrt{\frac{D\,t}{\Lambda^2}}\,\left(1-\frac{2}{3}\,r_p t+\mathcal{O}(r_p t)^2\right)-\frac{I_0\,r_p t}{i_0^{\mathcal{U}}-I_0}\,\left(1+\mathcal{O}(r_p t)\right)\\ &= \sqrt{\frac{D\,t}{\Lambda^2}}\,\left(1-\frac{I_0}{i_0^{\mathcal{U}}-I_0}\,\sqrt{\frac{r_p\,\Lambda^2}{D}}\,\sqrt{r_p t}-\frac{2}{3}\,r_p t+\mathcal{O}(r_p t)^{3/2}\right)\end{aligned} \tag{13}$$

In Figs. 7(a) and (b) we plot the left-hand side of Eq. (13) as function of t. The two panels refer to the two cell lines introduced in Fig. 2. The lines with different colors show the results of repeated experiments. In view of Fig. 5(a) we expect a square-root dependence, $\phi_-\,\sqrt{D/\Lambda^2}\,\sqrt{t}$. Hence, one can infer D based *only* on knowledge of the geometrical parameter Λ of the measurement region — provided that one clearly resolves the power law at early times. For the first cell line this is given. For the second cell line we do not recommend this analysis. However, for the provision of the reader we provide the power laws for the values obtained in [45] and those that will be derived in Sect. 4.2 by solid black and gray lines, respectively. A direct fit of the data (if successful) provides a value of D somewhere in between these two values (cf. Tab. 1).

Equation (13) entails that the corrections are small as long as

$$r_p t \ll \min\left(\frac{3}{2}\,;\;\frac{D}{r_p\Lambda^2}\,\left(\frac{i_0^{\mathcal{U}}}{I_0}-1\right)^2\right)$$

For the values of r_p and D of [45] the latter factors take the values 2.5 and 0.5, respectively. The fit should be performed for times earlier than 50 s and 15 s, respectively, when one requires that the corrections must be smaller than 5% of the leading contribution. This entails that the impact of the photobleaching in the second experiment can considerably be reduced by performing experiments with a stronger initial photobleaching, i.e. a smaller I_0.

In summary, this approach of data analysis can be applied when the range of data till the cutoff time spans at least one order of magnitude. The estimate of D will then only rely on knowledge of the expectation of the parameter Λ, i.e. on a geometric parameter characterizing the geometry of the ER in $\mathcal{F}$. When $|\mathcal{F}|$ and $|\partial\mathcal{F}|$ are measured for some structures it can most reliably be obtained based by inspecting the cumulative distribution function of $\Lambda=\sqrt{4\pi}\,|\mathcal{F}|/|\partial\mathcal{F}|$, as shown in Fig. 6(b).

4.2. Analysis Based on Eq. (11)

Equation (11) provides a slightly more involved data analysis that takes into account the impact of photobleaching during the experiments. It is based on the observation of Sect. 3.3 that the data collapse of Eq. (11) can be described as a cross-over of two power laws (cf. Fig. 6)

$$\frac{I(t)-I_0\,\mathrm{e}^{-r_p t}}{K} \simeq \frac{2\,\phi_-\,\phi_+\,\sqrt{r_p t}}{\phi_++2\,\phi_-\,r_p t} \tag{14a}$$

$$\Rightarrow \qquad I(t)=I_0\,\mathrm{e}^{-r_p t}+K\,\frac{2\,\phi_-\,\phi_+\,\sqrt{r_p t}}{\phi_++2\,\phi_-\,r_p t} \tag{14b}$$

Hence, for every given experimental data set we obtain K for a given r_p by fitting $I(t)$ with the right-hand side of Eq. (14b). In view of Eqs. (10) and (8) the variability of the values of K reflects to a substantial part the different structure of the ER in the measurement region. This is reflected in

Preprints (www.preprints.org) | NOT PEER-REVIEWED | Posted: 5 January 2024 doi:10.20944/preprints202401.0462.v1

the substantially improved data collapse shown in Fig. 7. In these plots we determine the preferred choice of r_p by looking for the best match of the fit (solid gray line) and the expectation of the data for the largest values of $r_p t$. In the present case this amounts to $r_p = 0.004(1)\,\mathrm{s}^{-1}$ for both data sets. This reflects the expectation that the quench rate is independent of the investigated cell line. It is a parameter set by the properties of the dye and the laser system of the setup. Accordingly, we find the best fits $D = 0.075(15)\,\mu\mathrm{m}^2/\mathrm{s}$ and $D = 0.034(13)\,\mu\mathrm{m}^2/\mathrm{s}$ for the data shown in Fig. 8(a) and (b), respectively. These regions are marked by green rectangles Fig. 8(c) and (d). The estimates for other quench rates are given by plus-symbols with error bars in those panels.

Moreover, in this figure the estimates suggested in Ref. [45] are shown by large squares. These estimates were obtained, however, for smaller values of r_p because the analysis of Ref. [45] is biased to provide the quench rates that are systematically too small.[4] On the other hand, Eq. (A1) and table (A5) of Ref. [45] provide a prediction of how the values of the diffusion coefficients change when adopting other values of r_p. It is shown by the solid lines shown in Fig. 8(c) and (d). For $r_p = 0.004\,\mathrm{s}^{-1}$ we find $D = 0.061\,\mu\mathrm{m}^2/\mathrm{s}$ and $D = 0.018\,\mu\mathrm{m}^2/\mathrm{s}$ for the first and second cell line, respectively. These values lie at the smaller side, but still within the error margins of the present analysis. They are shown by the small squares.

We believe that the present approach of the data analysis provides a more reliable estimates of r_p, which is based on the bending of the lines shown in Fig. 8(a) and (b). Moreover, it explicitly accounts for the substantial correlations of the structure of the ER in the measurement region and the observed FRAP signal, while [45] adopted a Bayesian average of the different diffusion coefficients encountered when aiming for a best match of the relaxation of measurement data and simulations performed for a different ER geometry. We believe that this is the origin of the slight difference of the present estimate and the values suggested in Ref. [45].

5. Discussion and Conclusion

We revisited a large body of highly-resolved numerical data addressing the diffusion of non-structural HCV proteins (NSPs) that are anchored in the endoplasmatic reticulum (ER). For the considered system we have access to structural information about the ER (Fig. 1), and to FRAP measurements (Fig. 2). We established scaling in the transport equations governing the diffusion process, and we inspected the resulting data collapse for all available numerical data (Fig. 6). The data falls on a master curve that is described to a very good approximation by Eq. (14).

Our analysis reveals that the geometrical structure and the topology of the ER in the FRAP measurement area have a severe impact on the evolution of the FRAP signal. Based on this insights we suggests a novel approach to analyze experimental data that is outlined in Sect. 4.2. This analysis is based on fitting experimental data, and it only requires information about the expectation value of a single parameter, Λ, that characterizes the geometry of FRAP measurement region: the parameter Λ amounts to the ratio of the surface area in the measurement region and the length of its boundary (Eq. (8)).

A very accurate quantitative evaluation of the diffusion constant is obtained in Fig. 8 by introducing corrections factors, $\phi_\pm$, that account for curvature and quenching effects. These factors take values close to one. In the present study they have been inferred by inspecting highly-resolved numerical data of the diffusive recovery for the diffusion on two-dimensional bicontinuous surfaces extracted from experimental measurements of the endoplasmatic reticulum (ER).

The present approach applies to the analysis of all FRAP signals of proteins that are anchored in the endoplasmatic reticulum or other biological structures with a complex two-dimensional shape. In a first approximation the fit function, Eq. (14a), can be adopted for the fits. The value of Λ appears in the fits through the definition of K, Eq. (10). The value of this ratio can be inferred from measurements

[4] It neglects diffusion of dye molecules into the test region considered in the estimate of r_p.

of the geometry of the ER by fluorescence imaging [25] or electrotomography [26]. The values of $\phi_{\pm}$ will likely not change a lot. However, for an accurate data analysis it will be worthwhile to perform a numerical study of new systems to adjust these empirical numerical factors in the fit function.

With this precaution one establishes a straightforward method to determine the diffusion parameters for viral proteins that are attached to the ER surface. These parameters can then be used in spatio-temporal resolved models of intracellular virus replication [44,47]. Moreover, the new data analysis can also be used to obtain the diffusion coefficients of arbitrary cell components that are located on the ER surface, such as specific metabolic proteins. These transport parameters are essential imputs to describe all diffusion-limited biochemical reactions rates in the spatially heterogeneous cell environments [54,55,61,62], in particular when the reactions take place on two-dimensional membranes [63].

Supplementary Materials: The following supporting information can be downloaded at the website of this paper posted on Preprints.org.

Author Contributions: MMK and GW developed the sufPDE model. MMK implemented the methods and performed the simulations. JV developed the scaling theory and the data analysis scheme. MMK and JV performed the data analysis and data interpretation. They also wrote the present manuscript. All the authors give their final approval of the article version to be published.

Funding: J.V. is grateful for the appointment as a Distinguished Visiting Professor at the Department of Mathematical Sciences of the Politecnico di Torino during the academic year 2016/17. It provided the opportunity to initiate the present work.

Acknowledgments: We are grateful to Alfio Grillo, with whom we spent several exciting nights where ideas were born that lead to the present paper. We thank Paul-Targett Adams and John McLauchlan, Glasgow BLA, for the permission to reuse their time series data [50]. MMK thanks Arne Nägel (MSQC Universität Frankfurt a.M.) for the very helpful discussions in the development of the sufPDE model and the implementation of the simulation code. He also acknowledges helpful discussions with Eva Herrmann (IBMM Universität Frankfurt a.M.) about the modeling of FRAP experiments. MMK thanks Wouter van Beerendonk (Huygens SVI, Netherlands) for his very friendly support in Huygens usage, backgrounds, and licensing. MMK acknowleges the HLRS Stuttgart for the supplied computing time at the HLRS Apollo Hawk supercomputer, where he performed the new simulations in the time when he was affiliated at the Goethe Center for Scientific Computing (GCSC) at Frankfurt University (2022).

Conflicts of Interest: The authors declare no conflict of interest.

Abbreviations

The following abbreviations are used in this manuscript:

PDE	Partial Differential Equation
sufPDE	surface PDE
ER	Endoplasmatic Reticulum
MW	membranous web
FRAP	fluorescence recovery after photobleaching
HCV	Hepatitis C virus
NSP	non structural protein
NS5a	non structural protein # 5a

References

1. Bakrania, S.; Chavez, C.; Ipince, A.; Rocca, M.; Oliver, S.; Stansfield, C.; Subrahmanian, R. Impacts of Pandemics and Epidemics on Child Protection: Lessons learned from a rapid review in the context of COVID-19. Technical report, UNICEF Office of Research - Innocenti, Florence, 2020.
2. World Health Organization. COVID-19 strategic preparedness and response plan: Monitoring and evaluation framework. Technical report, Geneva, 2021.
3. World Health Organization. 2021 Mid-Year Report: WHO Strategic action against COVID-19. Technical report, Geneva, 2021.

4. World Health Organization. Scoping review of interventions to maintain essential services for maternal, newborn, child and adolescent health and older people during disruptive events. Technical report, Geneva, 2021.
5. World Health Organization. Global Hepatitis Report 2017. Technical report, Geneva, 2017.
6. World Health Organization. WHO Strategic Response Plan: West Africa Ebola Outbreak. Technical report, Geneva, 2015.
7. Horvath, P.; Barrangou, R. CRISPR/Cas, the immune system of bacteria and archaea. *Science* **2010**, *327*, 167–170. https://doi.org/10.1126/science.1179555.
8. Barrangou, R.; Doudna, J.A. Applications of CRISPR technologies in research and beyond. *Nature Biotechnology* **2016**, *34*, 933–941. https://doi.org/10.1038/nbt.3659.
9. Powell, R.; Buchanan, A. Breaking Evolution's Chains: The Prospect of Deliberate Genetic Modification in Humans. *The Journal of Medicine and Philosophy: A Forum for Bioethics and Philosophy of Medicine* **2011**, *36*, 6–27. https://doi.org/10.1093/jmp/jhq057.
10. Baltimore, D.; Berg, P.; Botchan, M.; Carroll, D.; Charo, R.A.; Church, G.; Corn, J.E.; Daley, G.Q.; Doudna, J.A.; Fenner, M.; et al. A prudent path forward for genomic engineering and germline gene modification. *Science* **2015**, *348*, 36–38. https://doi.org/10.1126/science.aab1028.
11. Sinclair, A.; Islam, S.; Jones, S. Gene therapy: an overview of approved and pipeline technologies. Technical Report 171, CADTH, Ottawa, 2018.
12. Mullard, A. Gene-editing pipeline takes off. *Nature Reviews Drug Discovery* **2020**, *19*, 367–372. https://doi.org/10.1038/d41573-020-00096-y.
13. Vilchez, R.A.; Kozinetz, C.A.; Butel, J.S. Conventional epidemiology and the link between SV40 and human cancers. *Lancet Oncol.* **2003**, *4*, 188–191.
14. Liao, J.B. Viruses and Human Cancer. *Yale J Biol Med* **2006**, *79*, 115–122.
15. Lambert, P.F.; Sugden, B. Viruses and Human Cancer. In *Abeloff's Clinical Oncology*, 5th ed.; Niederhuber, J.E.; Armitage, J.O.; Dorshow, J.H.; Kastan, M.B.; Tepper, J.E., Eds.; Elsevier: Philadelphia, 2014; chapter 11.
16. Padariya, M.; Kalathiya, U.; Mikac, S.; Dziubek, K.; Fernandez, M.C.T.; Sroka, E.; Fahraeus, R.; Sznarkowska, A. Viruses, cancer and non-self recognition. *Open Biol.* **2021**, *11*, 200348. https://doi.org/10.1098/rsob.200348.
17. Miest, T.S.; Cattaneo, R. New viruses for cancer therapy: meeting clinical needs. *Nature Reviews Microbiology* **2014**, *12*, 23–34. https://doi.org/10.1038/nrmicro3140.
18. Fukuhara, H.; Ino, Y.; Todo, T. Oncolytic virus therapy: A new era of cancer treatment at dawn. *Cancer Science* **2016**, *107*, 1373–1379. https://doi.org/10.1111/cas.13027.
19. Ma, X.Y.; D.Hill, B.; Hoang, T.; Wen, F. Virus-inspired strategies for cancer therapy. *Seminars in Cancer Biology* **2021**, *in press*. https://doi.org/10.1016/j.semcancer.2021.06.021.
20. Hufnagel, L.; Brockmann, D.; Geisel, T. Forecast and control of epidemics in a globalized world. *PNAS* **2004**, *101*, 15124–15129. https://doi.org/10.1073/pnas.0308344101.
21. Deuffic, S.; Buffat, L.; Poynard, T.; Valleron, A.J. Modeling the hepatitis C virus epidemic in france. *Hepatology* **2003**. https://doi.org/10.1002/hep.510290528.
22. Monath, T.P.; Vasconcelos, P.F. Yellow fever. *Journal of Clinical Virology* **2015**, *64*, 160–173. https://doi.org/10.1016/j.jcv.2014.08.030.
23. Lowe, R.; Barcellos, C.; Cruz, O.G.; Honório, N.A.; Kuper, H.; Carvalho, M.S. The Zika Virus Epidemic in Brazil: From Discovery to Future Implications. *Int. J. Environ. Res. Public Health* **2018**, *15*, 96. https://doi.org/10.3390/ijerph15010096.
24. V'kovski, P.; Kratzel, A.; Steiner, S.; Stalder, H.; Thiel, V. Coronavirus biology and replication: implications for SARS-CoV-2. *Nature Review Microbiology* **2021**, *19*, 155–170. https://doi.org/10.1038/s41579-020-00468-6.
25. Targett-Adams, P.; Boulant, S.; McLauchlan, J. Visualization of double-stranded RNA in cells supporting hepatitis C virus RNA replication. *J. Virol.* **2008**, *82*, 2182–95.
26. Romero-Brey, I.; Merz, A.; Chiramel, A.; Lee, J.Y.; Chlanda, P.; Haselman, U.; Santarella-Mellwig, R.; Habermann, A.; Hoppe, S.; Kallis, S.; et al. Three-dimensional architecture and biogenesis of membrane structures associated with hepatitis C virus replication. *PLoS Path.* **2012**, *8*, e1003056.
27. Paul, D.; Bartenschlager, R. Architecture and biogenesis of plus-strand RNA virus replication factories. *Wo. J. Vir.* **2013**, *2*, 1–000.

28. Targett-Adams, P.; Graham, E.J.; Middleton, J.; Palmer, A.; Shaw, S.M.; Lavender, H.; Brain, P.; Tran, T.D.; Jones, L.H.; Wakenhut, F.; et al. Small molecules targeting hepatitis C virus-encoded NS5A cause subcellular redistribution of their target: insights into compound modes of action. *J. Virol.* **2011**, *85*, 6353–68.
29. Chukkapalli, V.; Berger, K.L.; Kelly, S.M.; Thomas, M.; Deiters, A.; Randall, G. Daclatasvir inhibits hepatitis C virus NS5A motility and hyper-accumulation of phosphoinositides. *Virology* **2015**, *476*, 168–179.
30. Wölk, B.; Büchele, B.; Moradpour, D.; Rice, C.M. A dynamic view of hepatitis C virus replication complexes. *J. Virol.* **2008**, *82*, 10519–31.
31. Eyre, N.S.; Fiches, G.N.; Aloia, A.L.; Helbig, K.J.; McCartney, E.M.; McErlean, C.S.P.; Li, K.; Aggarwal, A.; Turville, S.G.; Bearda, M.R. Dynamic imaging of the hepatitis C virus NS5A protein during a productive infection. *J. Virol.* **2014**, *88*, 3636–3652.
32. Welsch, S.; Miller, S.; Romero-Brey, I.; Merz, A.; Bleck, C.K.; Walther, P.; Fuller, S.D.; Antony, C.; Krijnse-Locker, J.; Bartenschlager, R. Composition and three-dimensional architecture of the dengue virus replication and assembly sites. *Cell Host Micr.* **2009**, *5*, 365–75.
33. Hoenen, T.; Biedenkopf, N.; Zielecki, F.; Jung, S.; Groseth, A.; Feldmann, H.; Becker, S. Oligomerization of Ebola Virus VP40 Is Essential for Particle Morphogenesis and Regulation of Viral Transcription. *J. Virol.* **2010**, *84*, 7053–7063.
34. Hoenen, T.; Shabman, R.S.; Groseth, A.; Herwig, A.; Weber, M.; Schudt, G.; Dolnik, O.; Basler, C.F.; Becker, S.; Feldmann, H. Inclusion Bodies Are a Site of Ebolavirus Replication. *J. Virol.* **2012**, *86*, 11779–11788.
35. Noda, T.; Ebihara, H.; Muramoto, Y.; Fujii, K.; Takada, A.; "et.al.". Assembly and budding of Ebolavirus. *PLoS Pathog* **2006**, *2*, e99. https://doi.org/10.1371/journal.ppat.0020099.
36. Stahelin, R.V. Membrane binding and bending in Ebola VP40 assembly and egress. *Front. Microbiol.* **2014**, *5*, 300. https://doi.org/10.3389/fmicb.2014.00300.
37. Bhattacharyya, S.; Hope, T.J. Full-length Ebola glycoprotein accumulates in the endoplasmic reticulum. *Virol. J.* **2011**, *8*, 11.
38. Bharat, T.; Noda, T.; Riches, J.; Kraehling, V.; Kolesnikovac, L.; Becker, S.; Kawaok, Y.; Briggs, J.A.G. Structural dissection of Ebola virus and its assembly determinants using cryo-electron tomography. *PNAS* **2012**, *109*, 4275–4280.
39. Frieman, M.; Yount, B.; Heise, M.; Kopecky-Bromberg, S.A.; Palese, P.; Baric, R.S. Severe Acute Respiratory Syndrome Coronavirus ORF6 Antagonizes STAT1 Function by Sequestering Nuclear Import Factors on the Rough Endoplasmic Reticulum/Golgi Membrane. *J. Virol.* **2007**, *81*, 9812–9824.
40. Olejnik, J.; Ryabchikova, E.; Corley, R.; Mühlberger, E. Intracellular Events and Cell Fate in Filovirus Infection. *Virus* **2011**, *3*, 1501–1531.
41. Pegoraro, G.; Bavari, S.; Panchal, R. Shedding Light on Filovirus Infection with High-Content Imaging. *Virus* **2012**, *4*, 1354–1371.
42. Schudt, G.; Kolesnikova, L.; Dolnik, O.; Sodeik, B.; Becker, S. Live-cell imaging of Marburg virus-infected cells uncovers actin-dependent transport of nucleocapsids over long distances. *PNAS* **2013**, *110*, 14402–14407.
43. Knodel, M.M.; Nägel, A.; Reiter, S.; Rupp, M.; Vogel, A.; Targett-Adams, P.; Herrmann, E.; Wittum, G. Multigrid analysis of spatially resolved hepatitis C virus protein simulations. *Computing and Visualization in Science* **2015**, *17*, 235–253. https://doi.org/10.1007/s00791-016-0261-7.
44. Knodel, M.M.; Reiter, S.; Targett-Adams, P.; Grillo, A.; Herrmann, E.; Wittum, G. 3D Spatially Resolved Models of the Intracellular Dynamics of the Hepatitis C Genome Replication Cycle. *Viruses* **2017**, *9*, 282. https://doi.org/10.3390/v9100282.
45. Knodel, M.M.; Nägel, A.; Reiter, S.; Rupp, M.; Vogel, A.; Targett-Adams, P.; McLauchlan, J.; Herrmann, E.; Wittum, G. Quantitative analysis of Hepatitis C NS5A viral protein dynamics on the ER surface. *Viruses* **2018**, *10*, 28.
46. Knodel, M.M.; Nägel, A.; Reiter, S.; Rupp, M.; Vogel, A.; Lampe, M.; Targett-Adams, P.; Herrmann, E.; Wittum, G. On Estimation of a Viral Protein Diffusion Constant on the Curved Intracellular ER Surface. In Proceedings of the High Performance Computing in Science and Engineering 15: Transactions of the High Performance Computing Center, Stuttgart (HLRS) 2015; Nagel, E.W.; Kröner, H.D.; Resch, M.M., Eds., Cham, 2016; pp. 641–657. https://doi.org/10.1007/978-3-319-24633-8_41.
47. Knodel, M.M.; Reiter, S.; Targett-Adams, P.; Grillo, A.; Herrmann, E.; Wittum, G. Advanced Hepatitis C Virus Replication PDE Models within a Realistic Intracellular Geometric Environment. *Int. J. Environ. Res. Public Health* **2019**, *16*, 513. https://doi.org/doi:10.3390/ijerph16030513.

48. Chatel-Chaix, L.; Bartenschlager, R. Dengue virus and Hepatitis C virus-induced replication and assembly compartments: The enemy inside - caught in the web. *J. Virol.* **2014**, *88*, 5907–11.
49. Moradpour, D.; Penin, F.; Rice, C.M. Replication of hepatitis C virus. *Nat. Rev. Microbiol.* **2007**, *5*, 453–463.
50. Jones, D.M.; Gretton, S.N.; McLauchlan, J.; Targett-Adams, P. Mobility analysis of an NS5A-GFP fusion protein in cells actively replicating hepatitis C virus subgenomic RNA. *J. Gen. Vir.* **2007**, *88*, 470–5.
51. Belda, O.; Targett-Adams, P. Small molecule inhibitors of the hepatitis C virus-encoded NS5A protein. *Vir. Res.* **2012**, *170*, 1–14.
52. Reits, E.A.J.; Neefjes, J.J. From fixed to FRAP: measuring protein mobility and activity in living cells. *Nat. Cell Biol.* **2001**, *3*, E145–E147.
53. Ishikawa-Ankerhold, H.C.; Ankerhold, R.; Drummen, G.P.C. Advanced Fluorescence Microscopy Techniques — FRAP, FLIP, FLAP, FRET and FLIM. *Mol.* **2012**, *17*, 4047–4132.
54. Lanoiselée, Y.; Moutal, N.; Grebenkov, D. Diffusion-limited reactions in dynamic heterogeneous media. *Nat Commun* **2018**, *9*. https://doi.org/10.1038/s41467-018-06610-6.
55. Sarkar, S. Concentration Dependence of Diffusion-Limited Reaction Rates and Its Consequences. *Phys. Rev. X* **2020**, *10*, 041032. https://doi.org/10.1103/PhysRevX.10.041032.
56. Fowler, A.C. *Mathematical Models in the Applied Sciences*; Cambridge Texts in Applied Mathematics, Cambridge UP: Cambbridge, UK, 1997.
57. Barenblatt, G.I. *Scaling*; Cambridge UP: Cambridge, UK, 2003.
58. Friedman, J.R.; Voeltz, G.K. The ER in 3D: a multifunctional dynamic membrane network. *Tr. in Cell Biol.* **2011**, *21*, 709.
59. Means, S.; Smith, A.J.; Shepherd, J.; Shadid, J.; Fowler, J.; Wojcikiewicz, R.J.H.; Mazel, T.; Smith, G.D.; Wilson, B.S. Reaction diffusion modeling of calcium dynamics with realistic ER geometry. *Biophysical Journal* **2006**, *91*, 537–557.
60. Morse, P.M.; Feshbach, H. *Methods of Theoretical Physics*; Vol. 1, *International Series in Pure and Applied Physics*, McGraw-Hill: New York, 1953.
61. Grima, R.; Schnell, S. A systematic investigation of the rate laws valid in intracellular environments. *Biophysical Chemistry* **2006**, *124*, 1–10. https://doi.org/10.1016/j.bpc.2006.04.019.
62. Boltz, H.H.; Sirbu, A.; Stelzer, N.; de Lanerolle, P.; Winkelmann, S.; Annibale, P. The Impact of Membrane Protein Diffusion on GPCR Signaling. *Cells* **2022**, *11*. https://doi.org/10.3390/cells11101660.
63. Yogurtcu, O.N.; Johnson, M.E. Theory of bi-molecular association dynamics in 2D for accurate model and experimental parameterization of binding rates. *J. Chem. Phys.* **2015**, *143*, 084117. https://doi.org/10.1063/1.4929390.